Chemical Science

ROYAL SOCIETY OF CHEMISTRY

EDGE ARTICLE

View Article Online
View Journal | View Issue

Cite this: *Chem. Sci.*, 2020, **11**, 2093

All publication charges for this article have been paid for by the Royal Society of Chemistry

Received 20th September 2019
Accepted 9th January 2020

DOI: 10.1039/c9sc04756e

rsc.li/chemical-science

A possible unaccounted source of atmospheric sulfate formation: amine-promoted hydrolysis and non-radical oxidation of sulfur dioxide†

Shixian Wang,[a] Xiao Cheng Zeng, *[ba] Hui Li *[a] and Joseph S. Francisco *[c]

Numerous field and laboratory studies have shown that amines, especially dimethylamine (DMA), are crucial to atmospheric particulate nucleation. However, the molecular mechanism by which amines lead to atmospheric particulate formation is still not fully understood. Herein, we show that DMA molecules can also promote the conversion of atmospheric SO_2 to sulfate. Based on *ab initio* simulations, we find that in the presence of DMA, the originally endothermic and kinetically unfavourable hydrolysis reaction between gaseous SO_2 and water vapour can become both exothermic and kinetically favourable. The resulting product, bisulfite $NH_2(CH_3)_2^+ \cdot HSO_3^-$, can be readily oxidized by ozone under ambient conditions. Kinetic analysis suggests that the hydrolysis rate of SO_2 and DMA with water vapour becomes highly competitive with and comparable to the rate of the reaction between SO_2 and OH•, especially under the conditions of heavily polluted air and high humidity. We also find that the oxidants NO_2 and N_2O_5 (whose role in sulfate formation is still under debate) appear to play a much less significant role than ozone in the aqueous oxidation reaction of SO_2. The newly identified oxidation mechanism of SO_2 promoted by both DMA and O_3 provides another important new source of sulfate formation in the atmosphere.

1 Introduction

Sulfuric acid in the atmosphere, mainly produced by the oxidation of gaseous sulfur dioxide, is known as the most important nucleating agent in the earliest stage of atmospheric new particle formation (NPF), as it possesses the lowest vapour pressure (<0.001 mmHg at 298 K) among the gaseous species in the atmosphere.[1–9] SO_2 in the atmosphere is mainly oxidized by OH• radicals produced from excited oxygen and water vapour.[10–12] However, numerous observations indicate that there is insufficient OH• to account for the unexpectedly rapid growth in H_2SO_4 concentration in the highly polluted atmosphere, in which the high aerosol concentration can actually block solar ultraviolet radiation and lower the concentration of OH• radicals, thereby preventing them from participating in photochemical reactions.[5] Moreover, OH• oxidation alone cannot explain the observed level of H_2SO_4 at nighttime.[13]

On the other hand, although the abundance of the common oxidizing gases O_3 and NO_x is much higher than that of OH• radicals in the atmosphere, previous *ab initio* calculations show that the direct oxidation of SO_2 by O_3/NO_x in the gas phase is kinetically unfeasible due to extremely high activation barriers. The hydrolysis of gaseous SO_2 is proposed as an alternative reaction pathway to yield H_2SO_4 because sulfurous acid can be more easily oxidized to sulfuric acid by some moderate oxidants, *e.g.*, ozone and NO_x.[14–17] However, the hydrolysis of SO_2 in the gas phase has also been shown to be both thermodynamically and kinetically unfavourable *via* high-level quantum mechanical (QM) calculations[10,18–20] since the hydrolysis of SO_2 with either H_2O monomer or dimer is an endothermic process and, again, entails very high energy barriers.[10] Hence, new oxidation pathways must be explored to explain the fast conversion of SO_2 to atmospheric H_2SO_4.

Atmospheric bases, such as ammonia (NH_3), are another important contributor to initial sulfate aerosols.[21] In addition, both cloud chamber studies and field measurements have revealed that atmospheric amines, especially dimethylamine (DMA), also play a surprisingly crucial role in the NPF process, even though their concentrations are two or three orders of magnitude lower than that of NH_3.[22–30] For example, Almeida *et al.* detected that a 5 pptv level of DMA can enhance the particle formation rate more than 1000-fold than 250 pptv NH_3.[8] More recently, Yao *et al.* reported that $H_2SO_4 \cdot DMA \cdot H_2O$ nucleation leads to high NPF rates in urban areas of China.[30] Li

[a]*Beijing Advanced Innovation Center for Soft Matter Science and Engineering, Beijing University of Chemistry Technology, Beijing 10029, China. E-mail: hli@mail.buct.edu.cn*

[b]*Department of Chemistry, University of Nebraska-Lincoln, Lincoln, Nebraska, USA 68588. E-mail: xzeng1@unl.edu*

[c]*Department of Earth and Environmental Sciences, University of Pennsylvania, Philadelphia, Pennsylvania, USA 19104. E-mail: frjoseph@sas.upenn.edu*

† Electronic supplementary information (ESI) available. See DOI: 10.1039/c9sc04756e

et al. found that sulfamic acid, produced from SO_3 and high concentrations of NH_3, can directly participate in $H_2SO_4 \cdot$DMA clustering.[31] Currently, it is widely accepted that DMA, similar to NH_3, can further stabilize sulfate clusters through salification with H_2SO_4. On the other hand, although Liu *et al.* showed that alkaline gases, such as ammonia, can promote the hydrolysis of SO_2 to form H_2SO_3 (ref. 22) and Chen *et al.* proposed that alkaline aerosols can trap SO_2, then being oxidized by NO_2,[14] the role played by DMA molecules in atmospheric chemistry is still incompletely understood, despite its fundamental importance for exploring the role of amines in atmospheric chemistry.

Here, we show that atmospheric amines can play a key role in the formation of sulfates at high relative humidity (RH) and low illumination, thereby contributing to enhanced aerosol formation on highly polluted days. *Ab initio* simulations demonstrate that the presence of methylamine (MA)/DMA molecules leads to exothermic hydrolysis of SO_2 with water vapour, without a barrier, to a product that can be oxidized by O_3 and NO_x. O_3 is also found to be a stronger oxidant than NO_x in the amine-assisted oxidation of SO_2. As a result, the concentration level of atmospheric H_2SO_4 from aqueous oxidation may be mainly controlled by the concentration of O_3 rather than that of NO_x. Based on transition state theory (TST) analysis and the observed concentrations of the participating atmospheric species, the rate of the SO_2 hydrolysis reaction with the assistance of DMA at 100% RH is even higher than the rate of SO_2 oxidization by OH•. This finding may shed new light on the long-standing endeavour to identify the unknown oxidation pathway leading to atmospheric sulfate formation.

2 Results and discussion

2.1 Hydrolysis of SO_2 assisted by DMA

The potential energy surfaces (PESs) for the hydrolysis reaction of SO_2, MA/DMA and $n H_2O$ (n = 1–3) are shown in Fig. 1(a–b) and S1 in ESI.† In the reaction with the water monomer (Fig. 1(a)), the breaking of the O–H bond of water in the presence of MA and DMA requires activation energies of 5.8 and 3.2 kcal mol^{-1}, respectively, indicating that both reactions can take place quite readily under ambient conditions. In contrast, the process of $SO_2 + H_2O \rightarrow H_2SO_3$ in the gas phase needs to overcome a high energy barrier of 33.9 kcal mol^{-1}.[12] Note that previous quantum-mechanical (QM) calculations showed that atmospheric ammonia can also lower the barrier for the hydrolysis of SO_2 to ~12.0 kcal mol^{-1}.[22] However, this energy barrier is still quite high for a reaction to take place at room temperature. According to our calculations, the hydrolysis barriers with MA and DMA are approximately 6.0 and 9.0 kcal mol^{-1} lower than the barrier with NH_3, respectively, suggesting that amines can promote SO_2 hydrolysis more strongly than NH_3. Furthermore, spontaneous ionization to form HSO_3^- and $NH_3CH_3^+$/$NH_2(CH_3)_2^+$ during the hydrolysis reactions is also observed.

The energy barrier for hydrolysis can be further lowered by introducing an additional water molecule to the reaction through

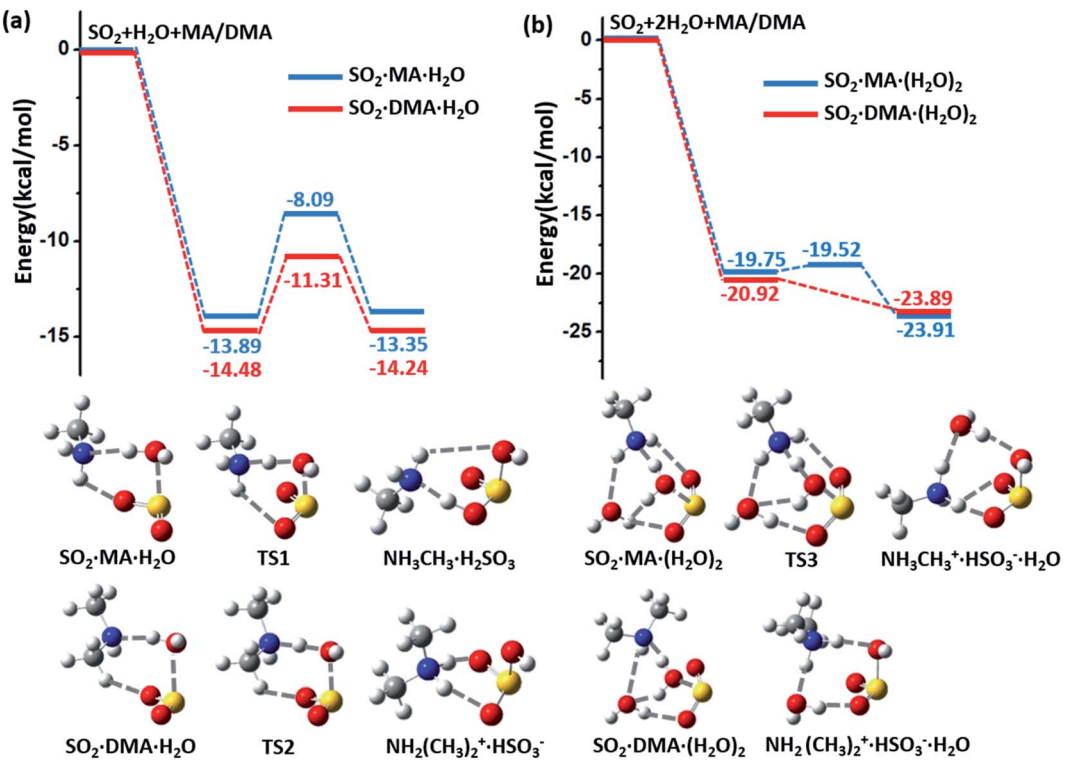

Fig. 1 (a) Potential energy profiles for the hydrolysis reactions of MA (blue lines)/DMA (red lines), SO_2, and H_2O monomer. (b) Potential energy profiles for the hydrolysis reactions of MA (blue lines)/DMA (red lines), SO_2, and H_2O dimer. The energy profiles are calculated at the M06-2X/cc-pVDZ-F12 level with zero-point-energy (ZPE) correction.

the formation of a ring structure in the transition state, as shown in Fig. 1(b). The hydrolysis of SO_2 with a water dimer and DMA can become barrierless. Likewise, hydrolysis with $(H_2O)_n$ ($n \geq 3$) are also barrierless reactions (ESI Fig. S1†). In addition, increasing the number of water and DMA molecules also promotes further ionization of the already formed H_2SO_3 and amine molecules. As shown in ESI Fig. S2†(a), H_2SO_3 is partially ionized to HSO_3^- in the $(DMA)_2 \cdot H_2SO_3 \cdot (H_2O)_n$, ($n$ = 1–3) clusters, while complete ionization of H_2SO_3 and DMA to $(NH_2(CH_3)_2^+)_2 \cdot SO_3^{2-}$ is observed in the presence of $(H_2O)_n$ ($n \geq 4$) with a very low dissociation barrier of 0.24 kcal mol^{-1} (ESI Fig. S2(b)†). Next, we show that the complete ionization of H_2SO_3 can benefit its oxidation, a phenomenon that may occur on aerosol surfaces (with high pH) in air with high concentrations of DMA and water.

The spontaneous formation and ionization processes of bisulfite/sulfite are confirmed by Born–Oppenheimer molecular dynamics (BOMD) simulation (Fig. 2). As shown by the BOMD trajectories at 300 K in Fig. 2(a), the hydrolysis of SO_2 with a water dimer and MA molecule is a very fast process, where the OH bond of a bridging water molecule breaks during the initial 0.33 ps of the BOMD simulation. Meanwhile, the N–H and O–S bond distances decrease to ~1.07 and ~1.78 Å, respectively, suggesting the formation of $NH_3CH_3^+ \cdot HSO_3^- \cdot H_2O$. It is observed that the system does not maintain the ionized form and returns back to the molecular state of SO_2 after 2.70 ps, indicating the reversible transition between SO_2 and HSO_3^- due to the thermal effect. It is interesting that such a chemical equilibrium can be sensitively regulated by temperature. The simulation system maintains the form of $NH_3CH_3^+ \cdot HSO_3^-$ at 300 K for ~2.4 ps during the total BOMD simulation time of 20 ps (lower panel in Fig. 2(b)), while the time period that $NH_3CH_3^+ \cdot HSO_3^-$ lasts is approximately six times longer at 250 K (~12.2 ps) than at 300 K (upper panel in Fig. 2(b)). The BOMD simulation of $SO_2 \cdot DMA \cdot (H_2O)_2$ shows a similar trajectory as that of the $SO_2 \cdot MA \cdot (H_2O)_2$ system (Fig. 2(c) and (d)), where the time periods of the $NH_2(CH_3)_2^+ \cdot HSO_3^-$ state are 9.1 and 10.6 ps at 300 and 250 K, respectively. Clearly, lower temperature is beneficial for bisulfite/sulfite formation due to its entropy being lower than that of the loose $SO_2 \cdot H_2O$ cluster.

Previous studies have suggested that heterogeneous reactions on the surface of water droplets play crucial roles in atmospheric chemistry, such as the ionization of N_2O_4.[32,33] Zhong *et al.* found that SO_2 on a water nanodroplet tends to have an S–O bond exposed to the air that can readily react with other gaseous species in the air.[34] Here, BOMD simulations also confirm that increasing the size of the water cluster can move the $SO_2 \leftrightarrow HSO_3^-$ equilibrium towards the right-hand side. As shown in ESI Fig. S3(a) and (b),† SO_2, MA/DMA, and two water molecules quickly convert to $NH_3CH_3^+/NH_2(CH_3)_2^+ \cdot HSO_3^- \cdot H_2O$ cyclic structures, which remain stable on the water cluster during the BOMD simulation at 300 K. By contrast, no similar structure is formed from SO_2 and NH_3 during the BOMD simulation (ESI Fig. S3(c)†), implying that the amines have a unique promotion effect on the hydrolysis of SO_2. The $NH_2(CH_3)_2^+ \cdot HSO_3^-$ complex on the water droplet can also uptake an additional DMA molecule to form $(NH_2(CH_3)_2^+)_2 \cdot SO_3^{2-}$, as shown in ESI Fig. S3(d).†

2.2 Oxidation of $NH_2(CH_3)_2^+ \cdot HSO_3^-$ and $(NH_2(CH_3)_2^+)_2 \cdot SO_3^{2-}$ by O_3

The oxidization process of $NH_2(CH_3)_2^+ \cdot HSO_3^-$ by O_3 is divided into two steps: (1) Adsorption of O_3 and (2) dissociation of $[SO_3 \cdot O_3H]^-$, as shown in the energy profiles in Fig. 3(a) and (b). The oxidation starts from the physical adsorption of O_3 with one oxygen atom approaching the HSO_3^- group (E_{ads} = −3.03 kcal mol^{-1}), and then the O_3 molecule is chemically adsorbed to HSO_3^- by forming a cyclic structure, $NH_2(CH_3)_2^+ \cdot$

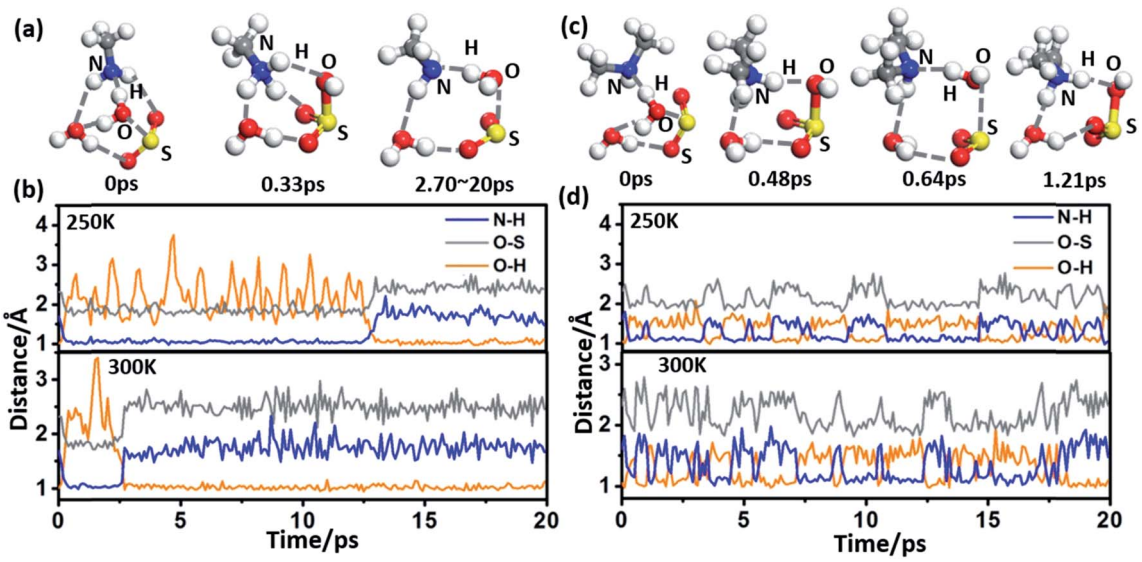

Fig. 2 (a) Snapshots taken from the BOMD simulation of $SO_2 \cdot MA \cdot (H_2O)_2$ at 300 K. (b) Time evolution of the O–H, O–S, and N–H bond lengths in $SO_2 \cdot MA \cdot (H_2O)_2$ at 250 and 300 K. (c) Snapshots taken from the BOMD simulation of $SO_2 \cdot DMA \cdot (H_2O)_2$ at 300 K. (d) Time evolution of the O–H, O–S, and N–H bond lengths in $SO_2 \cdot DMA \cdot (H_2O)_2$ at 250 and 300 K, respectively.

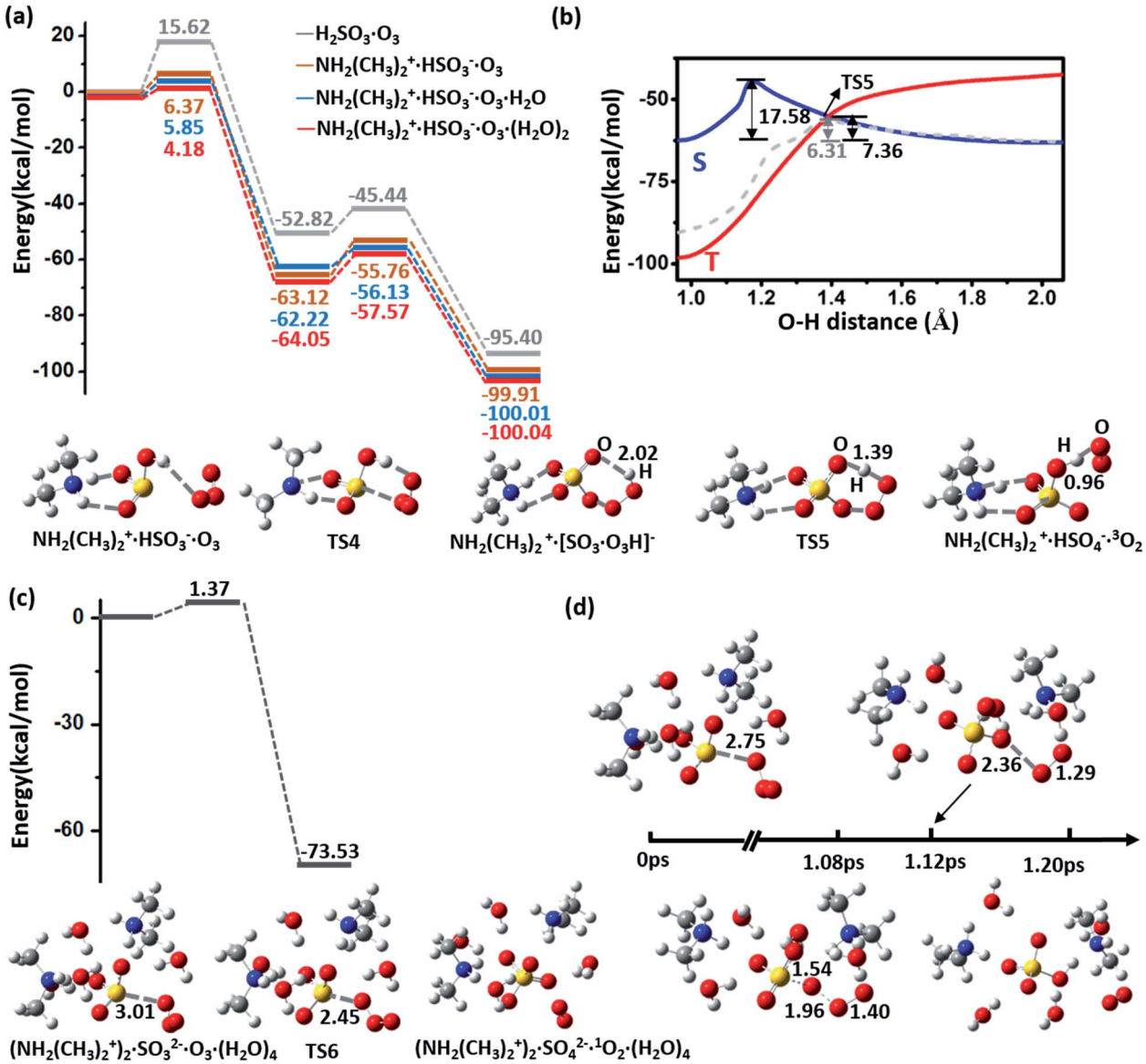

Fig. 3 (a) Potential energy profiles for the oxidation reactions of $H_2SO_3/CH_2(CH_3)_2^+ \cdot HSO_3^- \cdot (H_2O)_n$ ($n = 0, 1, 2$) and O_3. Snapshots are taken from the BOMD simulation. (b) Potential energy *versus* the O–H distance in $CH_2(CH_3)_2^+ \cdot [SO_3 \cdot O_3H]^-$. The blue and red lines correspond to the singlet and triplet multiplicities, respectively. The grey line is obtained from the spin-polarized calculation with the PBE functional in the VASP. Snapshots are taken from the BOMD simulation. (c) Potential energy profiles for the oxidation reactions of $(CH_2(CH_3)_2^+)_2 \cdot SO_3^{2-} \cdot (H_2O)_4$ and O_3. Snapshots are taken from the BOMD simulation. (d) Snapshots are taken from the BOMD simulation of $(CH_2(CH_3)_2^+)_2 \cdot SO_3^{2-} \cdot O_3 \cdot (H_2O)_4$ at 300 K. All energy profiles are calculated at the M06-2X/cc-pVDZ-F12 level with ZPE correction.

$[SO_3 \cdot O_3H]^-$, as an intermediate state. This process is highly exothermic ($\Delta E = -63.12$ kcal mol^{-1}) and overcomes a low barrier of 6.37 kcal mol^{-1}, which is 9.25 kcal mol^{-1} lower than the energy barrier without an amine (Fig. 3(a)). This energy barrier can be further lowered by adsorption of additional water molecules, where the energy barrier equals 5.85 and 4.18 kcal mol^{-1} for one and two H_2O molecules, respectively (Fig. 3(a)). Due to the low energy barrier, formation of the $NH_2(CH_3)_2^+ \cdot [SO_3 \cdot O_3H]^-$ complex can spontaneously occur during the BOMD simulation at room temperature (ESI Fig. S4†).

As $NH_2(CH_3)_2^+ \cdot [SO_3 \cdot O_3H]^-$ is an extremely stable intermediate state, the dissociation of $[SO_3 \cdot O_3H]^-$ needs to overcome a relatively high energy barrier ($E_a = 17.58$ kcal mol^{-1}) to produce HSO_4^- and singlet O_2 in the spin-restricted calculation (Fig. 3(b)). This barrier seems too high for a room–temperature reaction to occur. However, it is known that unstable singlet O_2 in the atmosphere can quickly convert to the triplet ground state[35] through collision and that, in particular, the strong spin–orbit interaction of the heavy element sulfur can greatly enhance the spin-flipping rate. Thus, the real dissociation process is accompanied by a spin-flipping process, which can greatly lower the dissociation barrier. Because the O–H stretching vibration corresponds to the main imaginary frequency of the transition state, we scan the energy surface *versus* the O–H distance (d_{OH}) of $[SO_3 \cdot O_3H]^-$, as shown in Fig. 3(b). The cross-point ($d_{OH} = 1.39$ Å) between the singlet and

triplet Born–Oppenheimer potential surfaces is found to yield a dissociation barrier of 7.36 kcal mol^{-1}, indicating the kinetic feasibility of the oxidation process under ambient conditions. The low dissociation barrier (E_a = 6.31 kcal mol^{-1}) is also confirmed by a calculation at the spin-polarized Perdew–Burke–Ernzerhof (PBE)/plane-wave level,[36] as implemented in the Vienna *Ab initio* Simulation Package (VASP 5.3).[37] The dissociation reaction is also highly exothermic (ΔE = −36.79 kcal mol^{-1}). Unlike the barrier to the adsorption of O_3, the dissociation barrier is minimally affected by additional vicinal water molecules (Fig. 3(a) and ESI Fig. S5†).

Moreover, the dissociation of HSO_3^- to SO_3^{2-}, which generally happens on alkaline aerosol surface, can promote oxidation with O_3. A cluster containing one H_2SO_3, two DMA, and four H_2O molecules is chosen to mimic this situation, where the DMA and H_2SO_3 molecules spontaneously form $NH_2(CH_3)_2^+$ and SO_3^{2-}. As shown in Fig. 3(c), the oxidation becomes a one-step reaction with an extremely low barrier (E_a = 1.37 kcal mol^{-1}). This oxidation process can be reproduced in the BOMD simulation as well (Fig. 3(d)).

2.3 Oxidation of $NH_2(CH_3)_2^+ \cdot HSO_3^-$ with NO_x

$NH_2(CH_3)_2^+ \cdot HSO_3^-$ can be oxidized by NO_2 to form the radical $NH_2(CH_3)_2^+ \cdot SO_3^-$ and HNO_2 (HONO) with an energy barrier of 13.08 kcal mol^{-1} and a potential energy change of −5.15 kcal mol^{-1}, as shown by the energy profiles and corresponding structures displayed in ESI Fig. 4(a) and S6(a),† respectively. In contrast to this oxidation reaction, the oxidation process without DMA has a relatively higher barrier (18.02 kcal mol^{-1}) and a positive energy change (6.30 kcal mol^{-1}), as shown in Fig. 4(a). Similar to the barrier for O_3 oxidation, the barrier for oxidizing $NH_2(CH_3)_2^+ \cdot SO_3^-$ with NO_2 can be lowered by extra neighbouring water molecules; *e.g.*, the values of the oxidation barrier in the presence of the water monomer and dimer are equal to 10.20 and 8.32 kcal mol^{-1}, respectively. Such a barrier is believed to be even lower on the surface of aqueous aerosols.

The $NH_2(CH_3)_2^+ \cdot SO_3^-$ radical product is an active radical, so it can easily react with other radicals, such as O_2, NO_2, and OH˙. For example, our calculations demonstrate that $NH_2(CH_3)_2^+ \cdot SO_3^- \cdot (H_2O)_n$ ($n \geq 1$) and another NO_2 molecule can spontaneously form a $NH_2(CH_3)_2^+ \cdot HSO_4^- \cdot (H_2O)_{n-1}$ cluster (ESI Fig. S6(b)†). In addition, HNO_2, the other product of this oxidation reaction, is also an important precursor of OH˙ radicals in the atmosphere.[38,39]

The potential energy profiles of $NH_2(CH_3)_2^+ \cdot HSO_3^- \cdot (H_2O)_n$ (n = 0–3) oxidized by N_2O_5, another abundant oxidative NO_x species in the atmosphere, are shown in Fig. 4(b) and ESI

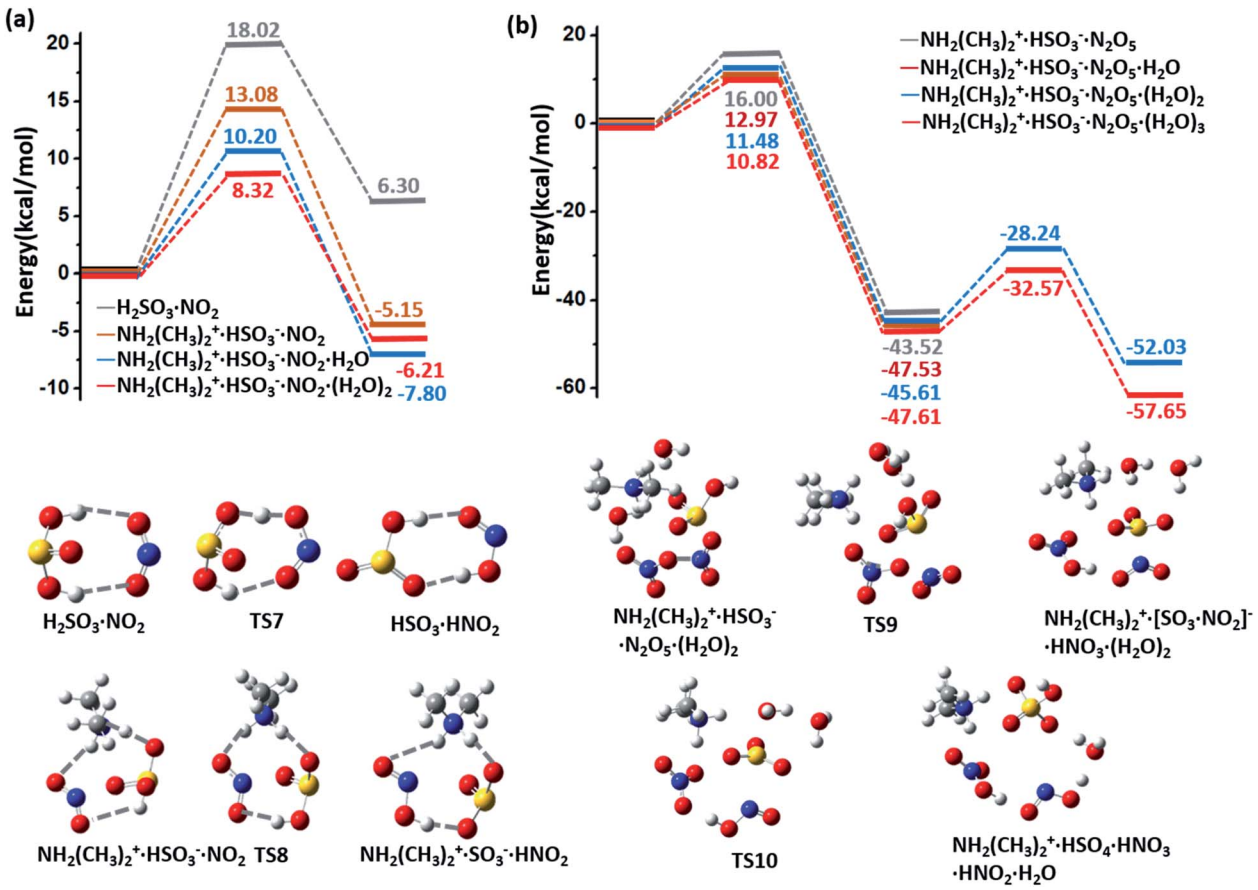

Fig. 4 (a) Potential energy profiles for the oxidation reactions of $H_2SO_3/CH_2(CH_3)_2^+ \cdot HSO_3^- \cdot (H_2O)_n$ and NO_2 (n = 0–2). (b) Potential energy profiles for the oxidation reaction for $H_2SO_3/NH_2(CH_3)_2^+ \cdot HSO_3^- \cdot (H_2O)_n$ (n = 0,1–3) and N_2O_5. The energy profiles are calculated at the M06-2X/cc-pVDZ-F12 level with ZPE correction. Snapshots are taken from the BOMD simulation.

Table 1 Values of the total rate constants (k, cm^3 $molecule^{-1}$ s^{-1}) for the hydrolysis reactions at temperatures from 240 to 300 K

	k (cm^3 $molecule^{-1}$ s^{-1})			
Reaction	240 K	260 K	280 K	300 K
$SO_2 \cdot H_2O$ + MA	6.56×10^{-13}	3.09×10^{-13}	1.58×10^{-13}	8.96×10^{-14}
$SO_2 \cdot H_2O$ + DMA	3.35×10^{-10}	9.42×10^{-11}	3.21×10^{-11}	1.39×10^{-11}
$SO_2 \cdot (H_2O)_2$ + MA	3.79×10^{-9}	3.17×10^{-9}	1.18×10^{-9}	4.22×10^{-10}
$SO_2 \cdot (H_2O)_2$ + DMA	9.01×10^{-9}	7.26×10^{-9}	5.64×10^{-9}	4.53×10^{-9}

Fig. S6(c).† Similar to O_3 oxidation, the process of $(NH_2(CH_3)_2^+ \cdot HSO_3^- \cdot (H_2O)_n + N_2O_5 \rightarrow CH_2(CH_3)_2^+ \cdot HSO_4^- \cdot (H_2O)_{n-1} + HNO_3 + HNO_2)$ is a two-step reaction, where N_2O_5 first dissociates into a $NO_2^- \cdot NO_3^+$ ion pair and combines with the bisulfite cluster to form a HNO_3 molecule and a stable complex $[SO_3 \cdot NO_2]^-$ (Fig. 4(b)). The energy barrier of this step also decreases from 16.0 to 10.82 kcal mol^{-1} as the number of participating water molecule increases (n = 0–3). In the second step, a H_2O molecule that attacks the sulfur atom will assist the breaking of $[SO_3 \cdot NO_2]^-$, and the product $CH_2(CH_3)_2^+ \cdot HSO_4^- \cdot HNO_3 \cdot HNO_2 \cdot (H_2O)_{n-1}$ is finally formed. This step is also an exothermic process (ΔE = −6.42 and −10.04 kcal mol^{-1} for n = 2 and 3, respectively), and the barrier of this step is weakly affected by the number of water molecules (E_a = 17.37 and 15.04 kcal mol^{-1} for n = 2 and 3, respectively). Such high energy barriers indicate that N_2O_5 plays a negligible role in the oxidation of sulfite.

2.4 Kinetics and implications for atmospheric chemistry

The reaction rate constants of hydrolysis reactions are calculated based on TST, as listed in Table 1, and details of this calculation and the reactant concentrations are listed in ESI Tables S1, S2 and S3.† The rate constant for the hydrolysis reaction of $SO_2 \cdot H_2O$ with DMA adopts an inverse relation with temperature, decreasing from 3.35×10^{-10} to 1.39×10^{-11} cm^3 $molecule^{-1}$ s^{-1} as the temperature changes from 240 to 300 K. According to previous observations, $[SO_2]$ and [DMA] are $\sim 10^{12}$ and $\sim 10^9$ molecules cm^{-3} in highly polluted air, respectively, while the concentration of H_2O decreases from 9.7×10^{17} to 9.0×10^{15} molecules cm^{-3} at 100% relative humility (RH) as the temperature drops from 300 K to 240 K.[7,30,40] On the basis of these parameters, the estimated concentrations of the $SO_2 \cdot H_2O$ and DMA·H_2O complexes at 300 K are approximately 3.4×10^8 and 1.9×10^6 molecules cm^{-3}, respectively, and the rate of hydrolysis for SO_2 and H_2O monomer assisted by DMA is estimated to be 4.8×10^6 molecule cm^{-3} s^{-1}.

It is interesting to compare the rate of SO_2 hydrolysis assisted by DMA to the rate of SO_2 reacting with OH• radicals under high RH conditions. The latter was previously thought to be the main reaction for SO_2 oxidation. Using the average concentration of OH• during the daytime (1×10^6 molecules cm^{-3}), the reaction rate of the oxidation of SO_2 by OH• based on a previously calculated rate constant (1.3×10^{-12} cm^3 $molecule^{-1}$ s^{-1} at 300 K and 1 atm)[41] is 1.5×10^6 molecule cm^{-3} s^{-1}, which is lower than the hydrolysis rate. In this case, the consumption of SO_2 in the hydrolysis reaction can exceed that in the oxidation reaction with OH• radicals. Similarly, the estimated hydrolysis rate for atmospheric SO_2, DMA, and $(H_2O)_2$ at 300 K and 100% RH is 2.9×10^6 molecules per cm^3 per s, which is also more competitive with the reaction rate of SO_2 and OH•. Moreover, the concentration of OH• would be further lowered due to the reduced photochemistry either during heavily polluted periods or at night time, when the hydrolysis reaction would even play an even more crucial role in SO_2 oxidation.

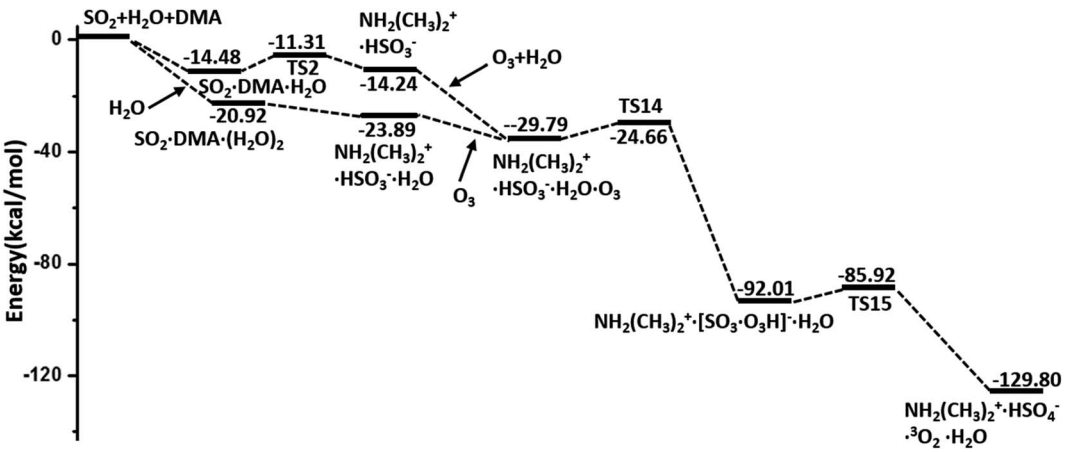

Fig. 5 Overall potential energy profiles for the hydrolysis of SO_2 promoted by DMA and oxidized by O_3 (M06-2X/cc-pVDZ-F12 with ZPE correction).

The hydration products $CH_2(CH_3)_2^+ \cdot HSO_3^- \cdot (H_2O)_n$ are expected to be oxidized by O_3, NO_2, and N_2O_5. The estimated rate constant of the oxidation of $CH_2(CH_3)_2^+ \cdot HSO_3^- \cdot (H_2O)_2$ by O_3 (5.82×10^{-15} cm^3 molecule^{-1} s^{-1}) is 3 orders of magnitude higher than that of the oxidation by NO_2 (1.73×10^{-18} cm^3 molecule^{-1} s^{-1}). As the concentrations of O_3, NO_2 and N_2O_5 were separately measured to be $\sim 10^{12}$, $\sim 10^{12}$, and $\sim 10^{10}$ molecules cm^{-3} in haze episodes, respectively,[7,42] we can estimate the lifetime of $CH_2(CH_3)_2^+ \cdot HSO_3^- \cdot (H_2O)_2$ by the expression $\tau = (k \times [\text{oxidant}])^{-1}$. The lifetime of $CH_2(CH_3)_2^+ \cdot HSO_3^- \cdot (H_2O)_2$ during oxidation by O_3 is $\sim$1/1000 of that during oxidation by NO_2 at 300 K. Considering the much lower oxidation rate constant and concentration of N_2O_5 than O_3 and NO_2, the oxidation by N_2O_5 is negligible. As a result, the proposed hydrolysis of SO_2 assisted by DMA in an O_3-polluted atmosphere is an important pathway for sulfate formation.

3 Conclusions

In summary, the hydrolysis and oxidation of SO_2 promoted by DMA are studied by using QM calculations and BOMD simulations. In both gaseous and heterogeneous environments, SO_2 can be easily hydrated with the assistance of DMA and then oxidized by O_3, as shown by the overall energy profile in Fig. 5. By contrast, NO_2 and N_2O_5, also viewed as important oxidants in the atmosphere, appear to play a much less important role than O_3 in the oxidation of SO_2. Kinetic analysis shows that the consumption rate of SO_2 during hydrolysis in the presence of DMA can surpass the rate of oxidation with OH• radicals under the conditions of heavily polluted air and high RH.

In the last decade, O_3 levels in the global atmosphere, according to field measurements, have greatly increased. For example, it has been reported that the yearly mean concentration of O_3 in Chinese megacities increased by 69% from 2006 to 2015.[43] The results from this research suggest that the hydrated oxidation of SO_2 with amines and O_3 has an important role in atmospheric chemistry.

4 Methods

4.1 Details of QM calculations and BOMD simulations

The geometries of the reactant states, transition states, and product states in all the reactions are optimized at the unrestricted M06-2X/cc-pVDZ-F_{12} level,[44–46] which has shown good results on weak interactions and has been widely used in computational studies of atmospheric chemistry.[16,46–48] Zero-point energy (ZPE) corrections are included when calculating the potential energies, and intrinsic reaction coordinate (IRC) analysis is carried out to confirm the reaction pathways. WB97XD/cc-pVDZ-F12 and B2PLYPD/def2-TZVP methods are also employed for the total potential energy profiles for comparison, which show great consistency with energy profiles based on M06-2X. All the QM calculations for the reaction pathways are performed by using the Gaussian 09 software package.[49] The spin-polarized calculations are performed based on the generalized gradient approximation of the PBE functional, as implemented in the VASP 5.3.[37,50–52] A kinetic energy cutoff of 400 eV is chosen for the plane-wave expansion. The cell size for the $NH_2(CH_3)_2^+ \cdot [SO_3 \cdot O_3H]$ cluster is $15 \times 15 \times 15$ Å^3.

BOMD simulations are performed in the framework of the Becke–Lee–Yang–Parr (BLYP) functional[53,54] with the Quickstep module in CP2K code.[55] The Gaussian and plane wave (GPW) basis sets (280 Ry energy cutoff) combined with the Goedecker-Teter-Hutter (GTH) pseudopotential[56] are employed to obtain a good balance between computational cost and accuracy. In addition, the dispersion correction is also included to better describe weak intermolecular interactions.[57] Periodic boundary conditions are used, and the cell sizes for the $SO_2 \cdot MA/DMA \cdot (H_2O)_2$, $NH_2(CH_3)_2^+ \cdot HSO_3^- \cdot O_3 \cdot (H_2O)_4$, and $(NH_2(CH_3)_2^+)_2 \cdot SO_3^{2-} \cdot O_3 \cdot (H_2O)_4$ systems are $20 \times 20 \times 20$ Å^3. A larger cell size ($35 \times 35 \times 35$ Å^3) is chosen for the hydrolysis reaction of SO_2 on the surface of a water nanodroplet containing 100 water molecules. The BOMD simulations are carried out at lower and higher temperatures (250 and 300 K), and the temperatures of the systems are controlled using the Nosé–Hoover thermostat. The time step of BOMD is set to 1.0 fs, which has been proven to achieve sufficient energy conservation for water systems.[34,47,58] The reaction process is unchanged with a smaller time step of 0.5 fs (ESI Fig. S7†).

4.2 Calculation of the reaction rate constant

The rate constants of hydrolysis and oxidation reactions are evaluated using TST with Wigner tunnelling corrections.[48,59,60] As $[SO_2][DMA]$ is negligible relative to $[SO_2][H_2O]$ and $[DMA][H_2O]$, in the hydrolysis reaction of SO_2 assisted by DMA, two reaction pathways are considered: H_2O first binding to SO_2 and first binding to DMA. Because the concentrations of the reactants DMA, SO_2, $SO_2 \cdot H_2O$, and $DMA \cdot H_2O$ are critical to the final reaction rates, we estimate the number of $SO_2 \cdot H_2O$ and $DMA \cdot H_2O$ complexes by the following expressions: $[SO_2 \cdot H_2O] = K_{SO_2 \cdot H_2O}[SO_2][H_2O]$ and $[DMA \cdot H_2O] = K_{DMA \cdot H_2O}[DMA][H_2O]$, where $K_{SO_2 \cdot H_2O}$ and $K_{DMA \cdot H_2O}$ are the equilibrium constants for the formation of $SO_2 \cdot H_2O$ and $DMA \cdot H_2O$ dimers, respectively. The total reaction rate ν can be expressed as

$$\begin{aligned} \upsilon_{SO_2 \cdot DMA \cdot H_2O} &= k_{SO_2 \cdot DMA \cdot H_2O}[SO_2 \cdot H_2O][DMA] \\ &= k'_{SO_2 \cdot DMA \cdot H_2O}[SO_2][DMA \cdot H_2O]. \end{aligned} \quad (1)$$

Taking the reaction of $SO_2 \cdot H_2O$ and DMA as an example, the hydrolysis process is represented by

$$SO_2 \cdot H_2O + DMA \underset{k_{-1}}{\overset{k_1}{\rightleftharpoons}} SO_2 \cdot DMA \cdot H_2O \xrightarrow{k_{uni}} DMA^+ \cdot HSO_3^- \quad (2)$$

By assuming that the reactant complex $SO_2 \cdot DMA \cdot H_2O$ is in equilibrium with the reactant monomers $SO_2 \cdot H_2O$ and DMA, the total rate constant $k_{SO_2 \cdot DMA \cdot H_2O}$ for the reaction can be written as

$$k_{SO_2 \cdot DMA \cdot H_2O} = \frac{k_1}{k_{-1}} k_{uni} = K_{eq} k_{uni} \quad (3)$$

where K_{eq} is the equilibrium constant for forming the reactant complex $SO_2 \cdot DMA \cdot H_2O$ and is expressed by

$$K_{eq} = \exp\left(-\frac{\Delta G_{eq}}{RT}\right) \quad (4)$$

where ΔG_{eq} is the free-energy change for the formation of the reactant complex, R is the gas constant, and T is the temperature. Here, k_{uni} is estimated by unimolecular TST and is expressed as

$$k_{uni} = \Gamma k_2 \quad (5)$$

The tunnelling effect factor Γ is given by Wigner tunnelling corrections,

$$\Gamma = 1 + \frac{1}{24}\left(\frac{h\overline{\nu^{+}}}{k_B T}\right)^2 \quad (6)$$

where h is the Planck constant, $\overline{\nu^{+}}$ is the imaginary frequency of the transition state, k_B is the Boltzmann constant, and k_2 is represented by

$$k_2 = \frac{k_B T}{h}\exp\left(-\frac{\Delta G}{RT}\right) \quad (7)$$

here, ΔG is the activation free-energy change from the reactant complex to the transition state. The entropic term S is obtained from the partition function $q(V,T)$ as

$$S = Nk_B + Nk_B \ln\left(\frac{q(V,T)}{N}\right) + Nk_B T\left(\frac{\partial q(V,T)}{\partial T}\right)_v \quad (8)$$

where $q(V,T)$ is determined from the calculation of vibrational frequency.

Conflicts of interest

There are no conflicts to declare.

Acknowledgements

We thank Dr Jinrong Yang for valuable discussions. HL is thankful for the funding support from the National Natural Science Foundation of China (21773005). JSF and XCZ acknowledge computer support from UNL Holland Computing Center.

Notes and references

1 F. Bianchi, J. Trostl, H. Junninen, C. Frege, S. Henne, C. R. Hoyle, U. Molteni, E. Herrmann, A. Adamov, N. Bukowiecki, X. Chen, J. Duplissy, M. Gysel, M. Hutterli, J. Kangasluoma, J. Kontkanen, A. Kurten, H. E. Manninen, S. Munch, O. Perakyla, T. Petaja, L. Rondo, C. Williamson, E. Weingartner, J. Curtius, D. R. Worsnop, M. Kulmala, J. Dommen and U. Baltensperger, *Science*, 2016, **352**, 1109–1112.

2 M. Kulmala, J. Kontkanen, H. Junninen, K. Lehtipalo, H. E. Manninen, T. Nieminen, T. Petaja, M. Sipila, S. Schobesberger, P. Rantala, A. Franchin, T. Jokinen, E. Jarvinen, M. Aijala, J. Kangasluoma, J. Hakala, P. P. Aalto, P. Paasonen, J. Mikkila, J. Vanhanen, J. Aalto, H. Hakola, U. Makkonen, T. Ruuskanen, R. L. Mauldin 3rd, J. Duplissy, H. Vehkamaki, J. Back, A. Kortelainen, I. Riipinen, T. Kurten, M. V. Johnston, J. N. Smith, M. Ehn, T. F. Mentel, K. E. Lehtinen, A. Laaksonen, V. M. Kerminen and D. R. Worsnop, *Science*, 2013, **339**, 943–946.

3 A. Kürten, F. Bianchi, J. Almeida, O. Kupiainen-Määttä, E. M. Dunne, J. Duplissy, C. Williamson, P. Barmet, M. Breitenlechner, J. Dommen, N. M. Donahue, R. C. Flagan, A. Franchin, H. Gordon, J. Hakala, A. Hansel, M. Heinritzi, L. Ickes, T. Jokinen, J. Kangasluoma, J. Kim, J. Kirkby, A. Kupc, K. Lehtipalo, M. Leiminger, V. Makhmutov, A. Onnela, I. K. Ortega, T. Petäjä, A. P. Praplan, F. Riccobono, M. P. Rissanen, L. Rondo, R. Schnitzhofer, S. Schobesberger, J. N. Smith, G. Steiner, Y. Stozhkov, A. Tomé, J. Tröstl, G. Tsagkogeorgas, P. E. Wagner, D. Wimmer, P. Ye, U. Baltensperger, K. Carslaw, M. Kulmala and J. Curtius, *J. Geophys. Res.: Atmos.*, 2016, **121**, 12377–12400.

4 R. Zhang, A. Khalizov, L. Wang, M. Hu and W. Xu, *Chem. Rev.*, 2012, **112**, 1957–2011.

5 Y. Cheng, G. Zheng, C. Wei, Q. Mu, B. Zheng, Z. Wang, M. Gao, Q. Zhang, K. He, G. Carmichael, U. Pöschl and H. Su, *Sci. Adv.*, 2016, **2016**, e1601530.

6 D. L. Yue, M. Hu, R. Y. Zhang, Z. B. Wang, J. Zheng, Z. J. Wu, A. Wiedensohler, L. Y. He, X. F. Huang and T. Zhu, *Atmos. Chem. Phys.*, 2010, **10**, 4953–4960.

7 G. J. Zheng, F. K. Duan, H. Su2, Y. L. Ma, Y. Cheng, B. Zheng, Q. Zhang, T. Huang, T. Kimoto, D. Chang, U. Pöschl, Y. F. Cheng and K. B. He, *Atmos. Chem. Phys.*, 2015, **2015**, 2969–2983.

8 J. Almeida, S. Schobesberger, A. Kurten, I. K. Ortega, O. Kupiainen-Maatta, A. P. Praplan, A. Adamov, A. Amorim, F. Bianchi, M. Breitenlechner, A. David, J. Dommen, N. M. Donahue, A. Downard, E. Dunne, J. Duplissy, S. Ehrhart, R. C. Flagan, A. Franchin, R. Guida, J. Hakala, A. Hansel, M. Heinritzi, H. Henschel, T. Jokinen, H. Junninen, M. Kajos, J. Kangasluoma, H. Keskinen, A. Kupc, T. Kurten, A. N. Kvashin, A. Laaksonen, K. Lehtipalo, M. Leiminger, J. Leppa, V. Loukonen, V. Makhmutov, S. Mathot, M. J. McGrath, T. Nieminen, T. Olenius, A. Onnela, T. Petaja, F. Riccobono, I. Riipinen, M. Rissanen, L. Rondo, T. Ruuskanen, F. D. Santos, N. Sarnela, S. Schallhart, R. Schnitzhofer, J. H. Seinfeld, M. Simon, M. Sipila, Y. Stozhkov, F. Stratmann, A. Tome, J. Trostl, G. Tsagkogeorgas, P. Vaattovaara, Y. Viisanen, A. Virtanen, A. Vrtala, P. E. Wagner, E. Weingartner, H. Wex, C. Williamson, D. Wimmer, P. Ye, T. Yli-Juuti, K. S. Carslaw, M. Kulmala, J. Curtius, U. Baltensperger, D. R. Worsnop, H. Vehkamaki and J. Kirkby, *Nature*, 2013, **502**, 359–363.

9 D. R. Hanson, *J. Geophys. Res.*, 2002, **107**, 4158.

10 W.-K. Li and M. L. McKee, *J. Phys. Chem. A*, 1997, **101**, 9778–9782.

11 J. J. Margitan, *J. Phys. Chem. A*, 1984, **88**, 3314–3318.

12 P. H. Wine, R. J. Thompson, A. R. Ravishankara, D. H. Semmes, C. A. Gump, A. Torabi and J. M. Nicovich, *J. Phys. Chem.*, 1983, **88**, 2095–2104.
13 R. L. Mauldin, T. Berndt, M. Sipila, P. Paasonen, T. Petaja, S. Kim, T. Kurten, F. Stratmann, V. M. Kerminen and M. Kulmala, *Nature*, 2012, **488**, 193–196.
14 Z. Chen, C. Liu, W. Liu, T. Zhang and J. Xu, *Sci. Total Environ.*, 2017, **575**, 429–436.
15 F. Sheng, L. Jingjing, C. Yu, T. Fu-Ming, D. Xuemei and L. Jing-yao, *RSC Adv.*, 2018, **8**, 7988–7996.
16 H. Zhang, S. Chen, J. Zhong, S. Zhang, Y. Zhang, X. Zhang, Z. Li and X. C. Zeng, *Atmos. Environ.*, 2018, **177**, 93–99.
17 J. Yang, L. Li, S. Wang, H. Li, J. S. Francisco, X. C. Zeng and Y. Gao, *J. Am. Chem. Soc.*, 2019, **141**, 19312–19320.
18 R. Steudel and Y. Steudel, *Eur. J. Inorg. Chem.*, 2009, **2009**, 1393–1405.
19 T. Loerting and K. R. Liedl, *J. Phys. Chem. A*, 2001, **105**, 5137–5145.
20 A. F. Voegele, C. S. Tautermann, C. Rauch, T. Loerting and K. R. Liedl, *J. Phys. Chem. A*, 2004, **108**, 3859–3864.
21 J. Kirkby, J. Curtius, J. Almeida, E. Dunne, J. Duplissy, S. Ehrhart, A. Franchin, S. Gagne, L. Ickes, A. Kurten, A. Kupc, A. Metzger, F. Riccobono, L. Rondo, S. Schobesberger, G. Tsagkogeorgas, D. Wimmer, A. Amorim, F. Bianchi, M. Breitenlechner, A. David, J. Dommen, A. Downard, M. Ehn, R. C. Flagan, S. Haider, A. Hansel, D. Hauser, W. Jud, H. Junninen, F. Kreissl, A. Kvashin, A. Laaksonen, K. Lehtipalo, J. Lima, E. R. Lovejoy, V. Makhmutov, S. Mathot, J. Mikkila, P. Minginette, S. Mogo, T. Nieminen, A. Onnela, P. Pereira, T. Petaja, R. Schnitzhofer, J. H. Seinfeld, M. Sipila, Y. Stozhkov, F. Stratmann, A. Tome, J. Vanhanen, Y. Viisanen, A. Vrtala, P. E. Wagner, H. Walther, E. Weingartner, H. Wex, P. M. Winkler, K. S. Carslaw, D. R. Worsnop, U. Baltensperger and M. Kulmala, *Nature*, 2011, **476**, 429–433.
22 J. Liu, S. Fang, W. Liu, M. Wang, F. M. Tao and J. Y. Liu, *J. Phys. Chem. A*, 2015, **119**, 102–111.
23 Y. You, V. P. Kanawade, J. A. de Gouw, A. B. Guenther, S. Madronich, M. R. Sierra-Hernández, M. Lawler, J. N. Smith, S. Takahama, G. Ruggeri, A. Koss, K. Olson, K. Baumann, R. J. Weber, A. Nenes, H. Guo, E. S. Edgerton, L. Porcelli, W. H. Brune, A. H. Goldstein and S. H. Lee, *Atmos. Chem. Phys.*, 2014, **14**, 12181–12194.
24 J. Zheng, Y. Ma, M. Chen, Q. Zhang, L. Wang, A. F. Khalizov, L. Yao, Z. Wang, X. Wang and L. Chen, *Atmos. Environ.*, 2015, **102**, 249–259.
25 M. Chen, M. Titcombe, J. Jiang, C. Jen, C. Kuang, M. L. Fischer, F. L. Eisele, J. I. Siepmann, D. R. Hanson, J. Zhao and P. H. McMurry, *Proc. Natl. Acad. Sci. U. S. A.*, 2012, **109**, 18713–18718.
26 C. Qiu, L. Wang, V. Lal, A. F. Khalizov and R. Zhang, *Environ. Sci. Technol.*, 2011, **45**, 4748–4755.
27 S. M. Murphy, A. Sorooshian, J. H. Kroll, N. L. Ng, P. Chhabra, C. Tong, J. D. Surratt, E. Knipping, R. C. Flagan and J. H. Seinfeld, *Atmos. Chem. Phys.*, 2007, **7**, 289–349.
28 H. Yu, R. McGraw and S.-H. Lee, *Geophys. Res. Lett.*, 2012, **39**, L02807.
29 C. Qiu and R. Zhang, *Phys. Chem. Chem. Phys.*, 2013, **15**, 5738–5752.
30 L. Yao, O. Garmash, F. Bianchi, J. Zheng, C. Yan., J. Kontkanen, H. Junninen, S. B. Mazon, M. Ehn, P. Paasonen, M. Sipilä, M. Wang, X. Wang, S. Xiao, H. Chen, Y. Lu, B. Zhang, D. Wang, Q. Fu, F. Geng, L. Li, H. Wang, L. Qiao, X. Yang, J. Chen, V.-M. Kerminen, T. Petäjä, D. R. Worsnop, M. Kulmala and L. Wang, *Science*, 2018, **361**, 278–281.
31 H. Li, J. Zhong, H. Vehkamaki, T. Kurten, W. Wang, M. Ge, S. Zhang, Z. Li, X. Zhang, J. S. Francisco and X. C. Zeng, *J. Am. Chem. Soc.*, 2018, **140**, 11020–11028.
32 B. J. Finlayson-Pitts, L. M. Wingen, A. L. Sumner, D. Syomin and K. A. Ramazan, *Phys. Chem. Chem. Phys.*, 2003, **5**, 223–242.
33 Y. Miller., B. J. Finlayson-Pitts and R. B. Gerber, *J. Am. Chem. Soc.*, 2009, **131**, 12180–12185.
34 J. Zhong, C. Zhu, L. Li, G. L. Richmond, J. S. Francisco and X. C. Zeng, *J. Am. Chem. Soc.*, 2017, **139**, 17168–17174.
35 C. Schweitzer and R. Schmid, *Chem. Rev.*, 2003, **103**, 1685–1757.
36 J. P. Perdew, K. Burke and M. Ernzerhof, *Phys. Rev. Lett.*, 1996, **77**, 3865–3868.
37 J. Furthmüller, J. Hafner and G. Kresse, *Phys. Rev. B: Condens. Matter Mater. Phys.*, 1994, **50**, 15606–15622.
38 A. J. M. Anglada, S. Olivella and A. Solé, *Phys. Chem. Chem. Phys.*, 2014, **16**, 19437–19445.
39 C. Ye, N. Zhang, H. Gao and X. Zhou, *Environ. Sci. Technol.*, 2017, **51**, 6849–6856.
40 M. E. Dunn, E. K. Pokon and G. C. Shields, *J. Am. Chem. Soc.*, 2003, **126**, 2647–2653.
41 B. Long, J. L. Bao and D. G. Truhlar, *Phys. Chem. Chem. Phys.*, 2017, **19**, 8091–8100.
42 H. Wang, K. Lu, X. Chen, Q. Zhu, Q. Chen, S. Guo, M. Jiang, X. Li, D. Shang, Z. Tan, Y. Wu, Z. Wu, Q. Zou, Y. Zheng, L. Zeng, T. Zhu, M. Hu and Y. Zhang, *Environ. Sci. Technol.*, 2017, **4**, 416–420.
43 W. Gao, X. Tie, J. Xu, R. Huang, X. Mao, G. Zhou and L. Chang, *Sci. Total Environ.*, 2017, **603–604**, 425–433.
44 C. Hattig, W. Klopper, A. Kohn and D. P. Tew, *Chem. Rev.*, 2012, **112**, 4–74.
45 G. Knizia, T. B. Adler and H. J. Werner, *J. Chem. Phys.*, 2009, **130**, 054104.
46 Y. Zhao and D. G. Truhlar, *Theor. Chem. Acc.*, 2008, **120**, 215–241.
47 J. Zhong, H. Li, M. Kumar, J. Liu, L. Liu, X. Zhang, X. C. Zeng and J. S. Francisco, *Angew. Chem., Int. Ed. Engl.*, 2019, **58**, 8351–8355.
48 R. Wu, S. Pan, Y. Li and L. Wang, *J. Phys. Chem. A*, 2014, **118**, 4533–4547.
49 M. J. Frisch, G. W. Trucks, H. B. Schlegel, G. E. Scuseria, M. A. Robb, J. R. Cheeseman, G. Scalmani, V. Barone, G. A. Petersson, H. Nakatsuji, X. Li, M. Caricato, A. Marenich, J. Bloino, B. G. Janesko, R. Gomperts, B. Mennucci, H. P. Hratchian, J. V. Ortiz, A. F. Izmaylov,

J. L. Sonnenberg, D. Williams-Young, F. Ding, F. Lipparini, F. Egidi, J. Goings, B. Peng, A. Petrone, T. Henderson, D. Ranasinghe, V. G. Zakrzewski, J. Gao, N. Rega, G. Zheng, W. Liang, M. Hada, M. Ehara, K. Toyota, R. Fukuda, J. Hasegawa, M. Ishida, T. Nakajima, Y. Honda, O. Kitao, H. Nakai, T. Vreven, K. Throssell, J. A. Montgomery Jr, J. E. Peralta, F. Ogliaro, M. Bearpark, J. J. Heyd, E. Brothers, K. N. Kudin, V. Staroverov, T. N. Keith, R. Kobayashi, J. Normand, K. Raghavachari, A. Rendell, J. C. Burant, S. S. Iyengar, J. Tomasi, M. Cossi, J. M. Millam, M. Klene, C. Adamo, R. Cammi, J. W. Ochterski, R. L. Martin, K. Morokuma, O. Farkas, J. B. Foresman and D. J. Fox, *Gaussian 09, Revision D.01*, Gaussian Inc., Wallingford, CT, 2009.

50 G. Kresse and J. Hafner, *Phys. Rev. B: Condens. Matter Mater. Phys.*, 1993, **47**, 558.

51 G. Kresse and J. FurthmüllerJ, *Comput. Mater. Sci.*, 1996, **6**, 15–50.

52 G. Kresse and J. Furthmuller, *Phys. Rev. B: Condens. Matter Mater. Phys.*, 1996, **54**, 11169–11186.

53 A. D. Becke, *Phys. Rev. A: At., Mol., Opt. Phys.*, 1988, **38**, 3098.

54 C. Lee, W. Yang and R. G. Parr, *Phys. Rev. B: Condens. Matter Mater. Phys.*, 1988, **37**, 785–789.

55 J. VandeVondele, F. Mohamed, M. Krack, J. Hutter, M. Sprik and M. Parrinello, *J. Chem. Phys.*, 2005, **122**, 14515.

56 G. Lippert, J. Hutter and M. Parrinello, *Mol. Phys.*, 2010, **92**, 477–488.

57 S. Grimme, J. Antony, S. Ehrlich and H. Krieg, *J. Chem. Phys.*, 2010, **132**, 154104.

58 C. Zhu, M. Kumar, J. Zhong, L. Li, J. S. Francisco and X. C. Zeng, *J. Am. Chem. Soc.*, 2016, **138**, 11164–11169.

59 J. Elm, S. Jorgensen, M. Bilde and K. V. Mikkelsen, *Phys. Chem. Chem. Phys.*, 2013, **15**, 9636–9645.

60 H. S. Johnston and J. Heicklen, *J. Chem. Phys.*, 1962, **66**, 532–533.

